Geophys. J. Int. (2003) **153,** 753–765

A comparison of subgrid-scale models for large-eddy simulations of convection in the Earth's core

Bruce A. Buffett*

Department of Earth and Ocean Sciences, University of British Columbia, Vancouver, BC V6T 1Z4, *Canada*

Accepted 2003 January 28. Received 2003 January 17; in original form 2002 July 5

SUMMARY

Large-eddy simulations provide a strategy for modelling large-scale flow when the smallest scales are not resolved. The approach relies on spatial filtering to eliminate scales smaller than the grid spacing, but requires models for the influence of the subgrid scales. We investigate four subgrid-scale models in numerical calculations of magnetoconvection in the Earth's core. Three of the models are based on eddy diffusivities, while the fourth is the similarity model of Bardina *et al.* (1980). The predictions of the subgrid-scale models are tested using a direct numerical simulation (DNS), which resolves the smallest dissipative scales. In order to achieve the required resolution we restrict the calculations to a small volume of the core with periodic boundary conditions. The grid is a cube with $128 \times 64 \times 32$ nodes, oriented so that the z-coordinate is aligned with the rotation axis and the y-coordinate is parallel to an imposed magnetic field. The direction of gravity may be oriented arbitrarily in the x–z plane and several representative cases are considered. Output from the DNS is filtered on to a coarser grid prior to evaluating the subgrid-scale models. The results are compared with estimates of the subgrid-scale heat and momentum fluxes calculated from the fully resolved solution. Substantial anisotropy in the subgrid-scale fluxes is caused by the influences of rotation and the imposed magnetic field. Models based on scalar eddy diffusivities are incapable of reproducing this anisotropy, whereas the similarity model gives a good match to the amplitude and spatial distribution of the subgrid-scale fluxes.

Key words: convection, dynamo theory, Earth's core, geomagnetism.

1 INTRODUCTION

Convection in the Earth's core occurs over a broad range of spatial scales. The largest spatial scales for fluid motion ($L \approx 10^6$ m) are imposed by the geometry of the core, whereas the smallest dissipative scales ($l < 10^{-1}$ m) are set by the low viscosity and chemical diffusivity of liquid iron alloys (Dobson 2000; Vocadlo *et al.* 2000). This vast range of spatial scales prevents direct simulation of convection-driven geodynamos (e.g. Roberts & Glatzmaier 2000). Instead, numerical modellers deal with the problem of limited spatial resolution by parametrizing processes that involve the subgrid scales (SGS). Strategies for dealing with SGS processes are often based on eddy diffusivities. Spatially constant eddy diffusivities and hyperdiffusivities are routinely used in numerical geodynamo models for computational expediency, although a more elaborate scheme have been devised to determined eddy diffusivities from the large-scale flow (see Lesieur & Métais 1996; Meneveau & Katz 2000, for recent reviews). Perhaps the best known example is the eddy-diffusivity model of Smagorinsky (1963), which is still widely used in many applications (e.g. Cantin *et al.* 2000).

Debate over the relative merits of constant diffusivities versus hyperdiffusivities (Zhang & Jones 1997; Grote *et al.* 2000) has demonstrated that differences in the SGS models can substantially influence the large-scale fields. These difficulties are compounded by the possibility that small-scale convection in the core is highly anisotropic due to the influence of rotation and a strong large-scale magnetic field (Braginsky & Meytlis 1990; St Pierre 1996; Shimizu & Loper 1997; Matsushima *et al.* 1999). Scalar diffusivities are inadequate for describing SGS processes in this case (Canuto & Cheng 1997). Few SGS models have been devised to deal with anisotropy, although the tensor diffusivity model of Matsushima (2001) is one exception. An alternative approach is the similarity model of Bardina *et al.* (1980), which relies on explicit filtering of the large-scale fields to estimate the SGS fluxes of heat and momentum. This method avoids the use of eddy diffusivities and yields anisotropic SGS fluxes when the large-scale fluxes are anisotropic.

The suitability of the similarity method for modelling convection in the Earth's core is tested using idealized calculations of magnetoconvection in a rapidly rotating fluid. Direct numerical simulations (DNS) reveal substantial anisotropy in the structure of small-scale

*Now at: Department of Geophysical Sciences, The University of Chicago, 5734 S. Ellis Avenue, Chicago IL 60637, USA. E-mail: buffett@geosci.uchicago.edu

convection, as reported previously in the numerical studies of St Pierre (1996) and Matsushima *et al.* (1999). Output from the DNS is filtered on to a coarser grid for use in the similarity model. Estimates of the SGS heat and momentum fluxes are compared with explicit calculations using the fully resolved (e.g. unfiltered) solution. Comparisons are also made with the Smagorinsky model and with models based on spatially constant eddy diffusivities and hyperdiffusivities. None of the eddy-diffusivity models yield satisfactorily estimates for the SGS fluxes. The spatial correlation between the predicted and calculated SGS fluxes is typical poor and occasionally negative. In contrast, the similarity method accounts for the strong anisotropy observed in the DNS and reproduces the spatial distribution of the SGS fluxes.

2 LARGE-EDDY SIMULATIONS

Large-eddy simulations (LES) use spatial filtering to eliminate scales that are smaller than the grid spacing Δ. Each field in the calculation (velocity $\mathbf{V}$, for example) is convolved with a filter function $G(\mathbf{x})$ to define the large-scale field (e.g. Leonard 1974)

$$\bar{\mathbf{V}}(\mathbf{x}, t) = \int G(\mathbf{x} - \mathbf{x}')\mathbf{V}(\mathbf{x}', t)\, d\mathbf{x}'. \tag{1}$$

Analogous expressions define the large-scale temperature $\overline{T}$ and magnetic field $\overline{\mathbf{B}}$ in the magnetoconvection calculations. The widely used Gaussian filter is expressed in one spatial dimension by

$$G_i(x_i) = \sqrt{\frac{6}{\pi}}\frac{1}{\Delta}\exp\left(-6x_i^2/\Delta^2\right). \tag{2}$$

The 3-D filter in eq. (1) is obtained by multiplying 1-D filters (e.g. $G(\mathbf{x}) = G_1(x_1)G_2(x_2)G_3(x_3)$). Another useful filter is

$$G_i(x_i) = \frac{2\sin(\pi x_i)/\Delta}{\pi x_i}, \tag{3}$$

which corresponds to a truncated Fourier expansion with wavenumbers $|k_i| < \pi/\Delta$.

Applying the filter to the governing equations yields a set of equations for the large-scale fields. To illustrate we filter the energy equation for an incompressible fluid

$$\frac{\partial T}{\partial t} + \mathbf{V}\cdot\nabla T = \kappa\nabla^2 T \tag{4}$$

to obtain

$$\frac{\partial \overline{T}}{\partial t} + \overline{\mathbf{V}}\cdot\nabla\overline{T} = \kappa\nabla^2\overline{T} - \nabla\cdot\mathbf{I}, \tag{5}$$

where

$$\mathbf{I} = \overline{\mathbf{V}T} - \overline{\mathbf{V}}\,\overline{T} \tag{6}$$

is the SGS heat flux. ($\mathbf{I}$ represents a correction for the omitted interactions between $\mathbf{V}$ and T when the large-scale heat flux is calculated from $\overline{\mathbf{V}T}$ instead of $\overline{\mathbf{V}}\,\overline{T}$.)

The SGS momentum flux emerges from the momentum equation in a similar way. The inertial non-linearity at large scales can be decomposed into two parts

$$\overline{\mathbf{V}\cdot\nabla\mathbf{V}} = \overline{\mathbf{V}}\cdot\nabla\overline{\mathbf{V}} + \nabla\cdot\boldsymbol{T}, \tag{7}$$

where

$$T_{ij} = \overline{V_iV_j} - \overline{V}_i\,\overline{V}_j \tag{8}$$

is the SGS momentum flux (or stress tensor). The same procedure is applied to all other non-linear terms in the equations governing magnetoconvection (see Section 4). These terms include the Lorentz force $\mathbf{B}\cdot\nabla\mathbf{B}/\mu$ in the momentum equation and $\nabla\times(\mathbf{V}\times\mathbf{B})$ in the magnetic induction equation. Applying the filter to the large-scale Lorentz force gives

$$\frac{1}{\mu}\overline{\mathbf{B}\cdot\nabla\mathbf{B}} = \frac{1}{\mu}(\overline{\mathbf{B}}\cdot\nabla\overline{\mathbf{B}} + \nabla\cdot\mathbf{M}), \tag{9}$$

where

$$M_{ij} = \overline{B_iB_j} - \overline{B}_i\,\overline{B}_j \tag{10}$$

is the SGS Maxwell stress. Similarly, the large-scale induction term is

$$\overline{\nabla\times(\mathbf{V}\times\mathbf{B})} = \nabla\times(\overline{\mathbf{V}}\times\overline{\mathbf{B}}) + \nabla\cdot\alpha, \tag{11}$$

where

$$\alpha_{ij} = (\overline{B_iV_j} + \overline{V_iB_j}) - (\overline{B}_i\overline{V}_j + \overline{V}_i\overline{B}_j) \tag{12}$$

is the SGS induction term. This term accounts for both generation and dissipation of the large-scale magnetic field by small-scale motion (Krause & Radler 1979; Moffatt 1970).

In order to implement the LES approach, we require models for each of the SGS terms in this section. Several models for the heat and momentum flux are described in Section 3. Discussion of the SGS Maxwell stress and induction terms is deferred until Section 6.

3 SGS MODELS

We turn now to the question of evaluating the SGS terms when only the large-scale fields are known. SGS processes are parametrized most commonly by means of eddy diffusivities. In some cases the eddy diffusivities are constant or depend on the wavenumber of the flow. In other cases the eddy diffusivities vary with the strain rate of the large-scale flow. Alternative approaches rely on explicit filtering of the large-scale fields. The similarity model of Bardina *et al.* (1980) applies a coarse filter to the large-scale (e.g. resolved) fields with the aim of approximating the SGS terms in Section 2. We summarize four commonly used SGS models in this section. Each of these models is subsequently tested using the output of a fully resolved numerical simulation.

3.1 Eddy-viscosity model

Eddy-viscosity (or diffusivity) models approximate the SGS processes by analogy with the effects of molecular viscosity (or diffusivity). Small-scale motions with velocity v and a characteristic length-scale l are parametrized in terms of an effective viscosity $\nu_t \approx vl$. A shortcoming of this analogy is the lack of separation between the large and small scales in turbulent flows. Normally, the distinction between the large and small scales is imposed by the choice of grid spacing in the numerical calculations. Near the scale of truncation the large (resolved) and small (unresolved) scales are comparable, so the analogy breaks down. Interactions between the large and small scales are liable to depend on their relative size, so we would not expect the effective viscosity to be constant across the resolved scales. In fact, numerical calculations in this study show that the eddy-viscosity model overestimates the influence of the SGS heat flux on the largest scales (see Section 5.1).

The scalar form of the eddy-viscosity model defines the deviatoric part of the stress tensor as

$$T_{ij} - \frac{1}{3}T_{kk}\delta_{ij} = -2\nu_t\overline{S}_{ij}\delta_{ij}, \tag{13}$$

where

$$\overline{S}_{ij} = \frac{1}{2}\left(\frac{\partial \overline{V}_i}{\partial x_j} + \frac{\partial \overline{V}_j}{\partial x_i}\right) \tag{14}$$

is the strain-rate tensor of the large-scale flow, ν_t is the eddy viscosity and δ_{ij} is the Kronecker delta. (The sign convection in (13) is customary in LES literature and follows from the definition of $\boldsymbol{T}$ in eq. (8).) Similarly, the SGS heat flux is defined in the eddy-diffusion approximation by

$$I_i = -\kappa_t \frac{\partial \overline{T}}{\partial x_i}, \tag{15}$$

where κ_t is the eddy diffusivity. Because the eddy viscosity and diffusivity are usually much larger than the molecular values, diffusion of heat and momentum are controlled by turbulent transport. When ν_t and κ_t are spatially constant, the resulting equations for the large-scale fields are indistinguishable from those in which the molecular diffusivities are increased to the turbulent values.

3.2 Hyperviscosity model

A variant of the eddy-viscosity model replaces derivatives in the dissipative terms with higher-order operators. The approach is called hyperviscosity because it enhances the damping of motion as the length-scale decreases. When the eddy viscosity in (13) is spatially constant, the effective body force on the large-scale flow can be written as

$$-\nabla \cdot \boldsymbol{T} = \nu_t \nabla^2 \overline{\mathbf{V}}. \tag{16}$$

Replacing ∇^2 with $-\nabla^4$, for example, is equivalent to replacing ν_t with an eddy viscosity that depends on the wavenumber of the motion. For a spectral method based on 3-D Fourier transforms, the effects of hyperdiffusion are included in the calculations by replacing ν_t with $\nu_t\, k^2$ in the Fourier-transformed equations. (k is the amplitude of the wavenumber vector.) A slightly modified form is adopted here to permit non-zero stress $\boldsymbol{T}$ and heat flux $\mathbf{I}$ in the presence of constant velocity and temperature gradients. The model for hyperviscosity and hyperdiffusion is

$$\nu_t(k) = \nu_0 \left[1 + A_\nu (k/k_c)^2\right] \tag{17}$$

$$\kappa_t(k) = \kappa_0 \left[1 + A_\kappa (k/k_c)^2\right], \tag{18}$$

where $k_c = \pi/\Delta$ is the cut-off wavenumber (or truncation) in the Fourier expansion, while ν_0, κ_0, A_ν and A_κ are constants.

Representations similar to those in eqs (17) and (18) are used in some geodynamo models (e.g. Glatzmaier & Roberts 1995, 1996; Kuang & Bloxham 1997, 1999). An important difference is that the wavenumber in the geodynamo models refers only to the angular part of the operator ∇^2 in spherical coordinates. This means that diffusion is handled differently in the horizontal and radial directions (Busse 2000; Grote *et al.* 2000), and this difference may give rise to anisotropy which is unrelated to the effects of rotation and a large-scale magnetic field. While there is some basis for hyperdiffusion in numerical geodynamo models (Buffett & Bloxham 2002), there is presently no reason to distinguish between the radial and horizontal directions.

3.3 Smagorinsky model

The model of Smagorinsky (1963) was originally devised for calculating large-scale atmospheric flow, although it is more widely used in engineering applications. The form of the eddy viscosity uses Δ as the characteristic length-scale and defines the characteristic velocity in terms of an invariant of the strain-rate tensor $\overline{S}_{ij}$ for the large-scale flow. The model gives

$$\nu_t = (C_S \Delta)^2 |\overline{\boldsymbol{S}}|, \tag{19}$$

where $|\overline{\boldsymbol{S}}| = (2\overline{S}_{ij}\overline{S}_{ij})^{1/2}$ and C_S is a constant. Lilly (1967) determined C_S by matching the kinetic energy dissipation of the Smagorinsky model with that predicted by a Kolmogorov spectrum in the inertial range. However, this estimate for C_S has little relevance for buoyancy-driven flow, so C_S is treated as an adjustable constant. The eddy diffusivity in the Smagorinsky model is

$$\kappa_t = Pr^{-1} (C_S \Delta)^2 |\overline{\boldsymbol{S}}|, \tag{20}$$

where $Pr = \nu_t/\kappa_t$ is the turbulent Prandtl number. Estimates for Pr are obtained from comparisons with the DNS.

3.4 Similarity model

Numerical simulations (Clarke *et al.* 1979) and experiments (Liu *et al.* 1994) show that the deviatoric part of the SGS stress tensor T_{ij} is not well correlated with the large-scale strain rate $\overline{S}_{ij}$ of a turbulent flow. These results highlight a limitation of eddy diffusivities and motivate the search for alternative strategies. Bardina *et al.* (1980) devised a scheme known as the similarity method, which relies on explicit filtering of the resolved fields. Their approach was later simplified and given its currently standard form by Germano (1986).

The similarity model is based on two assumptions: that the scales immediately below Δ have the greatest influence on the resolved flow, and that flow at scales below Δ is similar to that at scales immediately above Δ. In effect, the similarity method uses the structure of the resolved fields to infer the structure of the subgrid fields.

The SGS heat flux is approximated in the similarity model by (Germano 1986)

$$\mathbf{I} = C_I(\widetilde{\overline{\mathbf{V}}\,\overline{T}} - \widetilde{\overline{\mathbf{V}}}\,\widetilde{\overline{T}}), \tag{21}$$

where C_I is a constant and the tilde represents a second spatial filter with a width greater than Δ. To interpret eq. (21) it is instructive to consider how this estimate for $\mathbf{I}$ changes when the LES fields $\bar{\mathbf{V}}$ and $\bar{T}$ are replaced with the fully resolved fields $\mathbf{V}$ and T. The resulting estimate for $\mathbf{I}$ (with $C_I = 1$) is identical to the definition of the SGS heat flux on a coarser grid. The grid spacing is defined by the width of the second filter (say 2Δ). We cannot evaluate this estimate for $\mathbf{I}$ in practice because it includes contributions from scales below Δ. However, when these contributions are small compared with the contributions from scales between Δ and 2Δ, the approximation in eq. (21) provides a good estimate for the SGS heat flux on the coarser grid. The constant C_I is used to extrapolate $\mathbf{I}$ to a finer grid spacing (e.g. Δ) or to compensate for the neglect of flow at scales below Δ. Similar reasoning for the SGS stress tensor yields

$$T_{ij} = C_T(\widetilde{\overline{V}_i\,\overline{V}_j} - \widetilde{\overline{V}_i}\,\widetilde{\overline{V}_j}), \tag{22}$$

where C_T is a second constant.

We test these approximations and evaluate the constants using a fully resolved DNS. Output from the DNS is filtered on to a coarser grid by applying either a Gaussian or spectral truncation filter to $\mathbf{V}$, T and $\mathbf{B}$. This defines the resolved fields $\bar{\mathbf{V}}$, $\bar{T}$ and $\bar{\mathbf{B}}$ on the coarser grid. A second filter is applied to these fields when evaluating eqs (21) and (22). The results are compared with numerical estimates of eqs (6) and (8), which are evaluated using the fully resolved fields. Similar comparisons are made using the other SGS models described in this section.

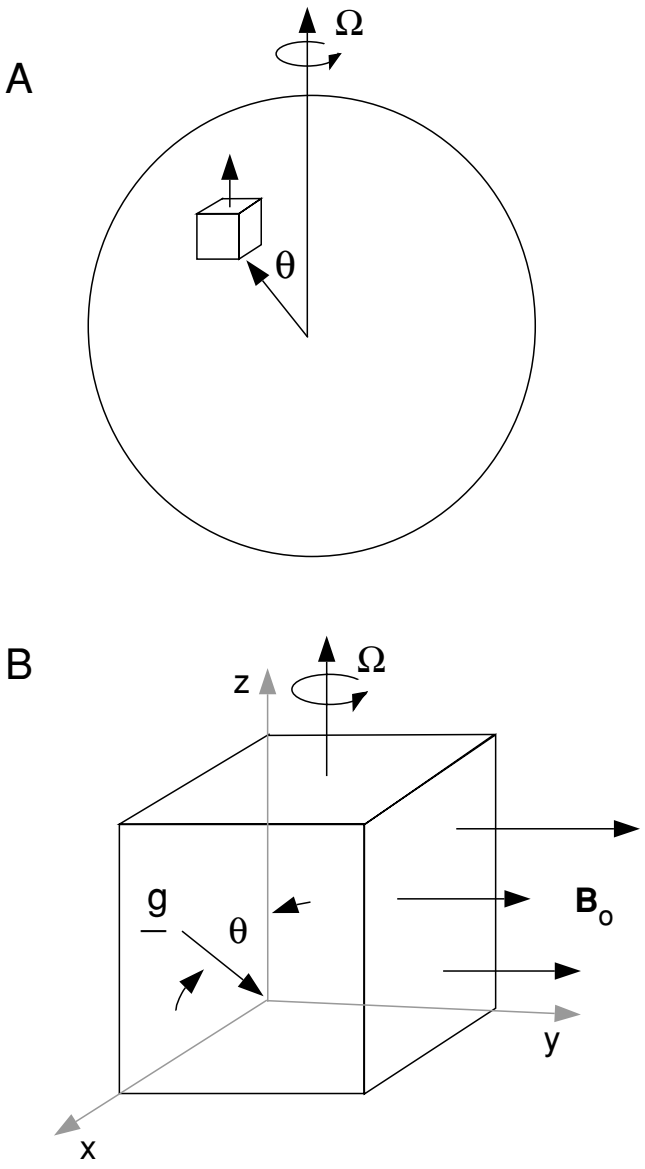

Figure 1. Schematic illustration of the computation volume (a) inside the liquid core and (b) in relation to the imposed magnetic field $\mathbf{B}_0$ and gravity **g**. The z-axis of the coordinate frame is aligned with the rotation vector Ω.

4 DIRECT NUMERICAL SIMULATION

In order to resolve the small dissipative scales in the DNS, we restrict our calculations to a small cube with periodic boundary conditions. The cube can be positioned anywhere in the interior of the core, although the grid is oriented with the z-coordinate aligned in the direction of the rotation axis and the y-coordinate aligned with an imposed magnetic field (Fig. 1). The geometry of the model is the same as that used by Matsushima *et al.* (1999). Because the imposed magnetic field is intended to represent the azimuthal field in the core, the gravity vector **g** is confined to the x–z plane; the orientation of **g** depends on the colatitude θ of the volume in the core. In one calculation we assume that **g** is parallel to the rotation vector Ω, corresponding to a volume in the polar regions of the core. A second calculation with $\theta = \pi/4$ represents a volume at mid-latitudes.

Convection is modelled in a rapidly rotating Boussinesq fluid. The governing equations are written in dimensionless form using the size of the cube as the length-scale l and the magnetic diffusion time l^2/η as the timescale. The imposed magnetic field $\mathbf{B}_0$ is used to scale the magnetic perturbation **B** and the initial temperature gradient ∇T_0 is parallel to the direction of gravity. The magnitude of the temperature gradient is $|\nabla T_0| = \beta$, and we use βl to scale the temperature perturbation T. The evolution equations for T, **B** and **V** are written in dimensionless form as (Braginsky & Roberts 1995)

$$\left(\partial_t - q\nabla^2\right)T = -\mathbf{V}\cdot\nabla T - \mathbf{V}\cdot\mathbf{1}_g \tag{23}$$

$$\left(\partial_t - \nabla^2\right)\mathbf{B} = \mathbf{1}_y\cdot\nabla\mathbf{V} + \nabla\times(\mathbf{V}\times\mathbf{B}) \tag{24}$$

$$Ro\left(\partial_t - P_m\nabla^2\right)\mathbf{V} = -\nabla P - \mathbf{1}_z\times\mathbf{V} - RaT\mathbf{1}_g - Ro(\mathbf{V}\cdot\nabla\mathbf{V}) + \Lambda(\mathbf{1}_y + \mathbf{B})\cdot\nabla\mathbf{B}, \tag{25}$$

where $\mathbf{1}_g$ is the unit vector in the direction of gravity and ($\mathbf{1}_x$, $\mathbf{1}_y$, $\mathbf{1}_z$) are the basis vectors of the coordinate system. (Coordinates x, y and z are used interchangably with x_1, x_2 and x_3.) In addition, we require

$$\nabla\cdot\mathbf{B} = \nabla\cdot\mathbf{V} = 0. \tag{26}$$

The dimensionless parameters include the magnetic Rossby number

$$Ro = \frac{\eta}{2\Omega l^2}, \tag{27}$$

the Rayleigh number

$$Ra = \frac{\alpha g\beta l^2}{2\Omega\eta} \tag{28}$$

and the Elsasser number

$$\Lambda = \frac{B_0^2\sigma}{2\Omega\rho}. \tag{29}$$

The viscosity ν and thermal diffusivity κ appear in the dimensionless equations through the magnetic Prandtl number $P_m = \nu/\eta$ and the Roberts number $q = \kappa/\eta$, respectively. We adopt molecular values for the viscosity and thermal diffusivity in the core so that we are not forced to make ad hoc assumptions concerning turbulent diffusivities in the DNS. The length-scale l and temperature gradient β are set to give a Rayleigh number which is twice the critical value (see Table 1). When we choose $l = 10^3$ m, the corresponding value of β yields an unstable density stratification, comparable to that inferred for the Earth's core by Braginsky & Meytlis (1990). Such small length-scales are necessary to obtained fully resolved calculations with molecular diffusivities. However, this does not restrict the validity of the SGS models to small scales. We could easily incorporate any of these SGS models into large-scale magnetoconvection calculations, but we would have no means of testing the

Table 1. Physical parameters for numerical calculation.

Parameter	Symbol	Value
Size of cube	l	1000 m
Rotation rate	Ω	0.73×10^{-4} s^{-1}
Imposed field	B_0	2 mT
Conductivity	σ	4×10^5 S m^{-1}
Mag. diffusivity	η	2 m^2 s^{-1}
Gravity	g	8 m s^{-2}
Thermal expansion	α	10^{-5} K^{-1}
Thermal gradient	β	8.0×10^{-9} K m^{-1} (a)
		6.6×10^{-9} K m^{-1} (b)

The thermal gradient is adjusted for cases (a) $\theta = 0$ and (b) $\theta = \pi/4$ to ensure that the Rayleigh number is twice the critical value.

SGS models. Instead, we prefer to test the SGS models under realistic conditions in the core, even though this makes the computation volume quite small.

The governing equations are solved by expanding **V**, **B** and T in Fourier series. The expansion for **V** is

$$\mathbf{V}(\mathbf{x}, t) = \sum_{\mathbf{k}} \mathbf{V}_k(t) \mathrm{e}^{i\mathbf{k}\cdot\mathbf{x}}, \tag{30}$$

where the wavenumber vector, $\mathbf{k} = (k_1, k_2, k_3)$, is truncated at $k_i = \pi/\Delta$ and $\mathbf{V}_k$ is the corresponding Fourier component. Similar representations for **B** and T yield Fourier components $\mathbf{B}_k$ and T_k, respectively. The Fourier-transformed equations become

$$\left(\partial_t + qk^2\right) T_k = f_k^T \tag{31}$$

$$\left(\partial_t + k^2\right) \mathbf{B}_k = ik_2 \mathbf{V}_k + \mathbf{f}_k^B \tag{32}$$

$$Ro\left(\partial_t + P_m k^2\right) \mathbf{V}_k = -i\mathbf{k} P_k + ik_2 \Lambda \mathbf{B}_k + \mathbf{f}_k^V, \tag{33}$$

where

$$f_k^T = -\mathbf{V}_k \cdot \mathbf{1}_g - (\mathbf{V} \cdot \nabla T)_k \tag{34}$$

$$\mathbf{f}_k^B = \nabla \times (\mathbf{V} \times \mathbf{B})_k \tag{35}$$

$$\mathbf{f}_k^V = \Lambda(\mathbf{B} \cdot \nabla \mathbf{B})_k - Ro(\mathbf{V} \cdot \nabla \mathbf{V})_k - RaT_k \mathbf{1}_g - \mathbf{1}_z \times \mathbf{V}_k. \tag{36}$$

Pressure is eliminated from eq. (33) by contracting with i **k** and using the condition $\mathbf{k} \cdot \mathbf{V}_k = \mathbf{k} \cdot \mathbf{B}_k = 0$ to obtain

$$P_k = -\frac{i\mathbf{k} \cdot \mathbf{f}_k^V}{k^2}. \tag{37}$$

The gradient in pressure is combined with all other terms on the right-hand side of eq. (33) to define a net forcing term, which we denote by $\mathbf{F}_k^V$. The forcing terms on the right-hand sides of eqs (31) and (32) are similarly denoted by F_k^T and $\mathbf{F}_k^B$, respectively. Allowances for remote boundaries are made by modifying $\mathbf{F}_k^V$. When the fluid is infinite, the geostrophic condition $\mathbf{1}_z \cdot \nabla \mathbf{V} = 0$ permits vertical motion that is independent of z. However, such flow is not permitted in a finite fluid because the velocity normal to the boundary must vanish. This condition is enforced in the numerical calculations by requiring $\mathbf{1}_z \cdot \mathbf{F}_k^V = 0$ when $k_3 = 0$.

Time stepping is done using integrating factors for the diffusion terms (e.g. Rogallo & Moin 1984), whereas all other terms are treated explicitly. Solutions for $T_k(t)$ and $\mathbf{V}_k(t)$ are advanced by directly integrating eqs (31) and (33) with imposed forcing terms F_k^T and $\mathbf{F}_k^V$. It is reasonable to assume that the integrating factors $\exp(qk^2 t)$ and $\exp(P_m k^2 t)$ are constant over one time step because q and P_m are small (see Table 2). When F_k^T and $\mathbf{F}_k^V$ are also assumed to be constant over one time step, we obtain

$$T_k(t + \Delta t) = T_k(t) \mathrm{e}^{-qk^2 \Delta t} + \Delta t \left[F_k^T(t)\right] \mathrm{e}^{-qk^2 \Delta t} \tag{38}$$

$$\mathbf{V}_k(t + \Delta t) = \mathbf{V}_k(t) \mathrm{e}^{-P_m k^2 \Delta t} + \frac{\Delta t}{Ro}\left[\mathbf{F}_k^V(t)\right] \mathrm{e}^{-P_m k^2 \Delta t}. \tag{39}$$

Little advantage is gained by using higher-order methods because sufficient accuracy is achieved with the short time step imposed by treating the Coriolis force explicitly. On the other hand, substantial improvements are possible if the integrating factor is generalized to include the effects of viscous and Coriolis forces in the integration for $\mathbf{V}_k(t)$. (Tests show that this method of solution is about 20 times faster in this particular application.) The induction equation is handled differently because the magnetic diffusivity is not small. When the integrating factor $\exp(k^2 t)$ is included in the integral over one time step, the solution for $\mathbf{B}_k(t)$ becomes

$$\mathbf{B}_k(t + \Delta t) = \mathbf{B}_k(t) \mathrm{e}^{-k^2 \Delta t} + \frac{1}{k^2}\left(1 - \mathrm{e}^{-k^2 \Delta t}\right) \mathbf{F}_k^B(t). \tag{40}$$

The non-linear terms in F_k^T, $\mathbf{F}_k^V$ and $\mathbf{F}_k^B$ are evaluated using a pseudospectral method (Orszag 1971). We first evaluate the fields **V**, **B** and T on a finer grid ($196 \times 96 \times 48$) by padding the Fourier transforms $\mathbf{V}_k$, $\mathbf{B}_k$ and T_k with zeros and transforming the expanded representation to the spatial domain. The non-linear terms are then calculated in the spatial domain and the result is transformed to the spectral domain. De-aliasing of the non-linear terms is done using the 3/2 rule (e.g. Canuto *et al.* 1988), which reduces the effective grid to $128 \times 64 \times 32$.

The numerical accuracy of the method is assessed by evaluating the energy balance every 100 time steps. The buoyancy flux, $RaT\,\mathbf{V} \cdot \mathbf{1}_g$, is integrated over the volume of the grid and compared with the sum of the energy sinks, which include the ohmic and viscous losses, and the rates of change of kinetic and magnetic energy. (The rates of change of magnetic and kinetic energy are evaluated using three successive time steps.) The error in the energy balance relative to the buoyancy flux is typically 10^{-5}.

Fig. 2 shows the temporal evolution of the net buoyancy flux and ohmic dissipation from a representative calculation with $\theta = 0$. The energy released by the motion of buoyant fluid is almost completely balanced by ohmic losses. Viscous losses are much smaller, and mainly associated with geostrophic flow in the direction of the imposed magnetic field. Short-wavelength variations in the geostrophic flow produce large rates of shear. However, the viscosity of the fluid is low enough to prevent the viscous losses from contributing significantly to the energy balance.

Small fluctuations in the buoyancy flux are evident in the expanded view of Fig. 2. These fluctuations are due to inertial waves that advect temperature anomalies through the gravity field (Zhang 1994). There is no evidence of oscillations in the ohmic dissipation, which means that the waves do not distort the imposed magnetic field. This restriction on the form of the inertial waves is probably the result of magnetic damping. Waves that distort the imposed magnetic field are so heavily damped by ohmic losses that they are not excited to observable levels. Those waves that are evident in Fig. 2 propagate in directions that do not cause significant distortion of the imposed field. (These waves are characterized by wavenumbers with $k_2 = 0$.) Small fluctuations in the buoyancy flux due to these waves are superimposed on a much larger variation due to quasi-steady motion of thermal anomalies. Whether the inertial waves influence the quasi-steady motion is not readily apparent from the DNS because it is not possible to isolate one effect from the other in the DNS. However, it may be possible to gain insights into this question by repeating the calculations with an implicit time-stepping method that filters inertial waves. Small differences in the quasi-steady motion would imply that inertial oscillations have only a small influence on convection.

The influences of rotation and an imposed magnetic field cause substantial anisotropy in the structure of convection. Fig. 3 shows isosurfaces of the temperature perturbation at $T = 0.4$ (red) and $T = -0.4$ (blue) from a sequence of perspectives. Each image is identified by the angle ϕ between the line of sight and the y-axis. The

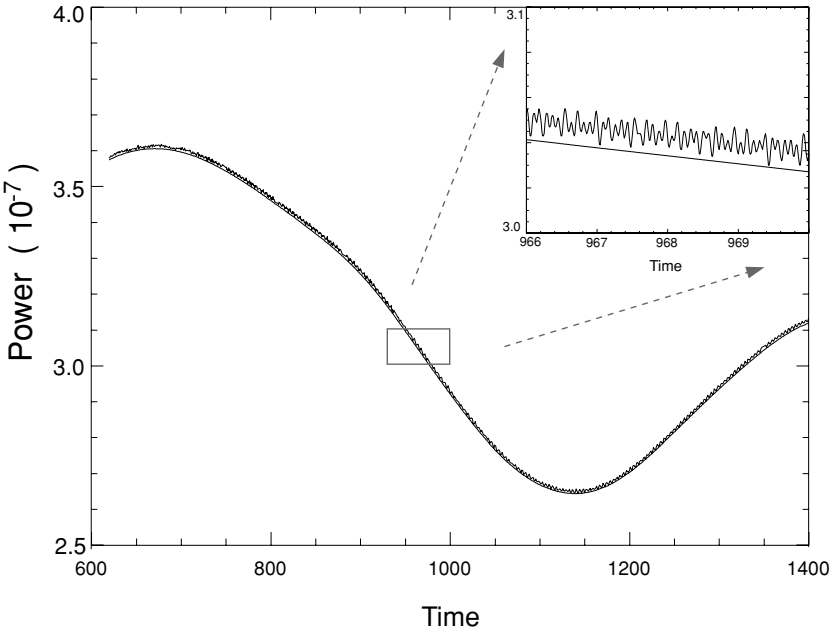

Figure 2. Time variations in the net buoyancy flux and ohmic dissipation from a representative calculation with $\theta = 0$. The inset highlights the oscillations in the buoyancy flux due to inertial waves. No oscillations are evident in the ohmic dissipation, which means that these waves do not distort the imposed magnetic field. Suppression of the waves that distort the imposed magnetic field is due to the heavy damping by ohmic dissipation, which keeps the amplitude of these waves small.

image in Fig. 3(a) with $\phi = 0$ shows a view along the y-axis. This perspective reveals narrow regions of warm and cold fluid, which extend in the direction of the rotation axis. As the line of sight shifts it becomes clear that these temperature anomalies have a plate-like structure with an orientation in the y–z plane. This structure is consistent with the predictions of Braginsky & Meytlis (1990), and accounts for the finer numerical resolution required in the x-direction.

Power spectra for T, $\mathbf{B}$ and $\mathbf{V}$ are shown in Fig. 4 as a function of k_1. These 1-D spectra are obtained by summing the power in wavenumbers k_2 and k_3 at a given value of k_1. Calculations with $\theta = 0$ and $\pi/4$ yield spectra with broadly similar amplitude and shape. Differences in the position of the peak of $\mathbf{V}_k$ reflect differences in the wavenumber of the most unstable mode. All wavenumbers above $k_1 \approx 16$ are stable to convection, so temperature anomalies at larger wavenumbers are due to non-linear transfers from large scales to small. The low viscosity and thermal diffusivity of the fluid permit temperature anomalies to cascade well beyond the spatial limit of convective instabilities.

We use the long-wavelength part of the DNS in the next section to evaluate the SGS models. Each field is filtered on to a coarser grid by applying either a Gaussian or spectral truncation filter. The filtered fields $\bar{\mathbf{V}}$, $\bar{\mathbf{B}}$ and $\bar{T}$ serve as inputs for evaluating the SGS models. The predictions are compared with estimates of the SGS heat flux and stress calculated using eqs (6) and (8), respectively. Numerical comparisons show that the choice of filter (either Gaussian or spectral truncation) has little influence on the predictions of the SGS models. However, the choice of filter does influence the SGS quantities calculated using eqs (6) and (8). When the spectral truncation filter is used in eqs (6) and (8), the SGS heat flux and stress exhibit spatial ringing, which is not evident in the estimates obtained using the Gaussian filter. Fortunately, these differences become small when we confine our comparison to the short-wavelength part of the SGS estimates. More specifically, spatial correlations between the different estimates improve substantially when these estimates are high-pass filtered before comparison. This is encouraging because the SGS heat flux and stress have the greatest influence on the smallest resolved scales, and this is where the choice of filter has the smallest influence. For the purpose of testing the SGS models in the next section, we apply a Gaussian filter with $\Delta = \pi/32$ to evaluate the SGS heat flux and stress in eqs (6) and (8). Representative examples are shown in Fig. 5, where the vertical heat flux I_3 and the shear stress T_{12} are plotted on a horizontal surface through the middle of the volume. Root-mean-square (rms) amplitudes for I_i and the shear components of T_{ij} are listed in Table 3. These results are compared with the predictions of the SGS models in the next section.

5 COMPARISON OF SGS MODELS

The SGS models in Section 3 are evaluated using the fields $\bar{\mathbf{V}}$, $\bar{\mathbf{B}}$ and $\bar{T}$, which are defined by applying a Gaussian filter with $\Delta = \pi/32$ to the fully resolved solution. Tests are also performed using fields that are filtered with $\Delta = \pi/16$, although the results are qualitatively similar to those obtained with $\Delta = \pi/32$. In this section we make detailed comparisons of the SGS models computed using a truncation at $\Delta = \pi/32$ and tabulate the results for the coarser grid.

5.1 Predictions of the eddy-viscosity model

The SGS stress is parametrized in the eddy-viscosity model by an effective viscosity ν_t, which depends on a characteristic length and velocity for the SGS flow. The grid spacing $\Delta = \pi/32$ is the natural choice for the characteristic length and the kinetic energy of the SGS flow is used to define a velocity. With these definitions the turbulent viscosity and diffusivity are $\nu_t = \kappa_t = 7 \times 10^{-5}$.

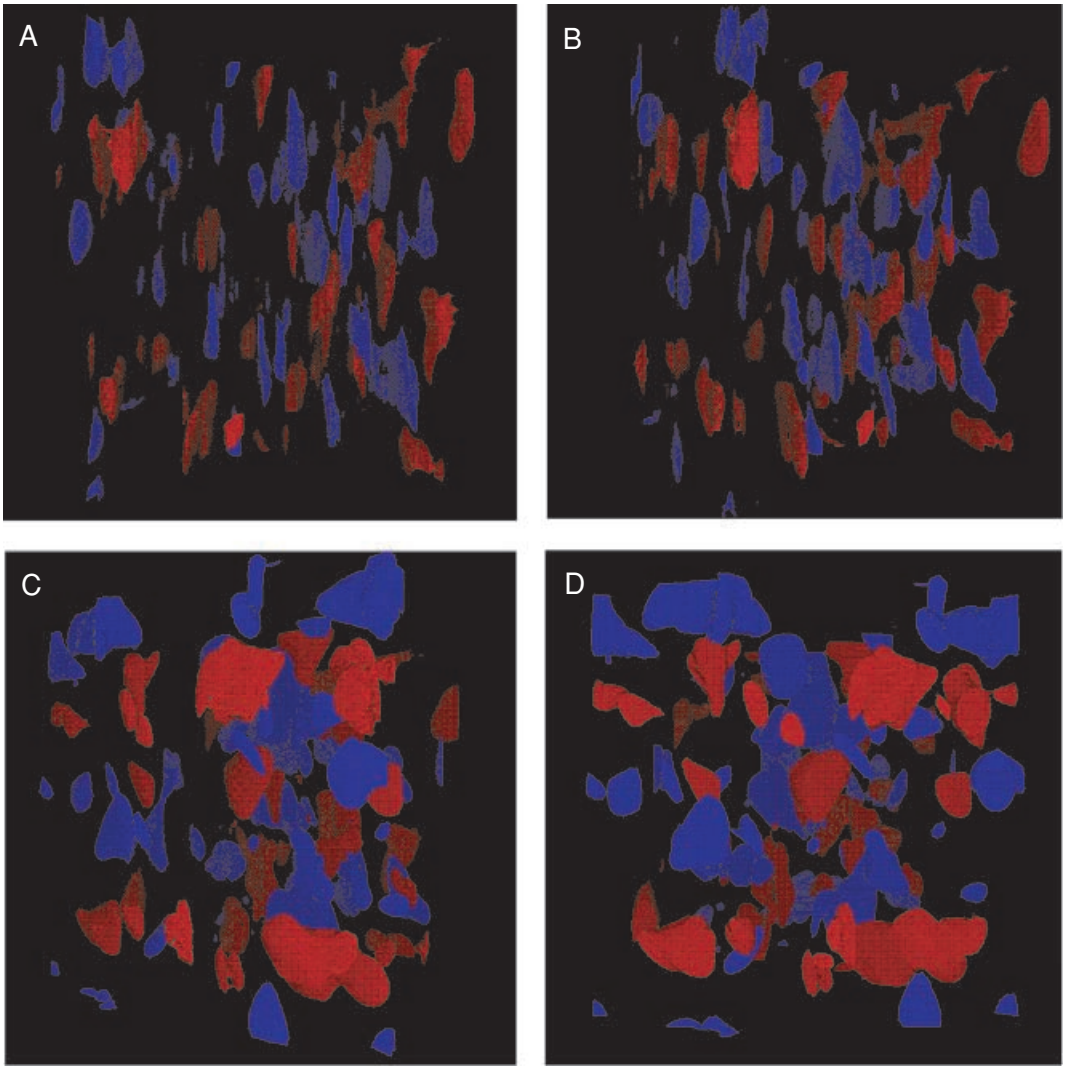

Figure 3. Isosurfaces of temperature perturbation at $T = 0.4$ (red) and $T = -0.4$ (blue). A sequence of perspectives are identified by the angle ϕ between the line of sight and the y-axis. We show (a) $\phi = 0$, (b) $\phi = \pi/6$, (c) $\phi = \pi/3$ and (d) $\phi = \pi/2$. The view from $\phi = 0$ is along the y-axis. As ϕ increases, the point of view shifts towards the x-axis. Plate-like temperature anomalies are oriented in the y–z plane.

The shear stress T_{12} predicted with the eddy-viscosity model is shown in Fig. 6(a). By definition, the spatial distribution of the predicted shear stress reflects the strain rate of the large-scale flow. The narrow regions of T_{12} in this prediction imply narrow bands of shear in the direction of the y-axis, probably associated with the geostrophic component of flow. Similar patterns of shear stress are evident in the SGS estimate (Fig. 5a), although the amplitude of the two results differ by a factor of 4. In addition, the location of positive (black) and negative (white) regions of T_{12} are misaligned. Consequently, the spatial correlation γ between the model prediction and the SGS shear stress is poor ($\gamma = -0.23$).

Fig. 7(a) shows the vertical heat flux I_3 predicted with the eddy-diffusion model. Broad regions of positive (upward) heat flux are predicted on a weaker background flux. In contrast, the SGS estimate (Fig. 5b) has more small-scale structure, and even regions where the heat flux is negative. The spatial correlation between the model prediction and the SGS heat flux is surprisingly good ($\gamma = 0.40$), especially considering the differences in the spatial variability of I_3. Much of this correlation is due to the long-wavelength part of I_3. When the long-wavelength part I_3 is isolated by filtering wavenumbers $k_i > 16$ from both the eddy-diffusion model and the SGS estimate, the correlation increases to $\gamma = 0.52$. Conversely, when the short-wavelength part of I_3 is isolated by filtering wavenumbers $k_i < 16$, the correlation decreases to $\gamma = -0.11$. Poor correlation at short wavelengths is a problem because the SGS estimates have their greatest influence on this part of the solution. In contrast, the long-wavelength part of the solution is governed mainly by the resolved scales, so the SGS model has much less direct influence at larger scales.

A second issue is the relative amplitude of SGS predictions at large and small scales. The net vertical heat flux in the eddy-diffusion model is nearly equal to the vertical heat flux in the SGS estimate, despite the differences in spatial variability. Most of the heat flux in the eddy diffusion model occurs at long wavelengths, whereas the explicit calculation of I_3 gives a larger fraction of the heat flux at shorter wavelengths. This indicates that the eddy-diffusion model overestimates the SGS heat flux at long wavelengths and underestimates the heat flux at shorter wavelengths. This is precisely the shortcoming that hyperdiffusion is intended to correct (Glatzmaier 2002).

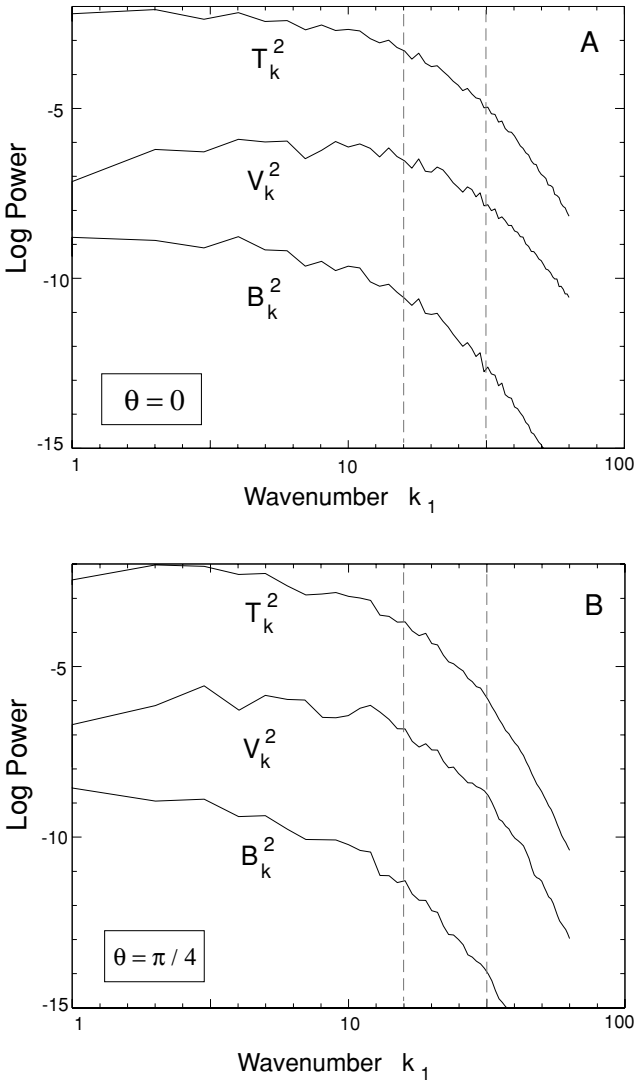

Figure 4. 1-D power spectra for T, **V** and **B** from representative calculations with (a) $\theta = 0$ and (b) $\theta = \pi/4$. The vertical (dashed) lines indicate the position of a spectral truncation at $\Delta = \pi/32$ and $\Delta = \pi/16$.

5.2 Predictions of the hyperviscosity model

Eq. (17) for ν_t in the hyperviscosity model depends on the amplitude A_ν of the scale dependence and the effective viscosity ν_0 at long wavelength. Predictions for T_{12} are made using $A_\nu = 10$ and $\nu_0 = 1.1 \times 10^{-5}$, which ensures that the rms variation in T_{12} is equal to that obtained using the eddy-viscosity model in Section 5.1. The predicted stress (Fig. 6b) is remarkably similar to the stress predicted with the eddy-viscosity model (Fig. 6a). This similarity can be explained by noting that the strain rate $\overline{S}_{12}$ is associated with a narrow range of spatial scales, so that the consequences of a scale-dependent viscosity are not discernible. In fact, the spatial correlation between the eddy-viscosity and the hyperviscosity models is $\gamma = 0.9$. It follows that both models have equally poor spatial correlation with the SGS estimate of stress (Table 4).

The influence of a scale-dependent diffusivity is much more evident in the prediction of the vertical heat flux (Fig. 7b). Use of hyperdiffusion emphasizes short-wavelength features in the heat flux, and even produces regions where the heat flux is negative. The Fourier components of the predicted heat flux have amplitudes

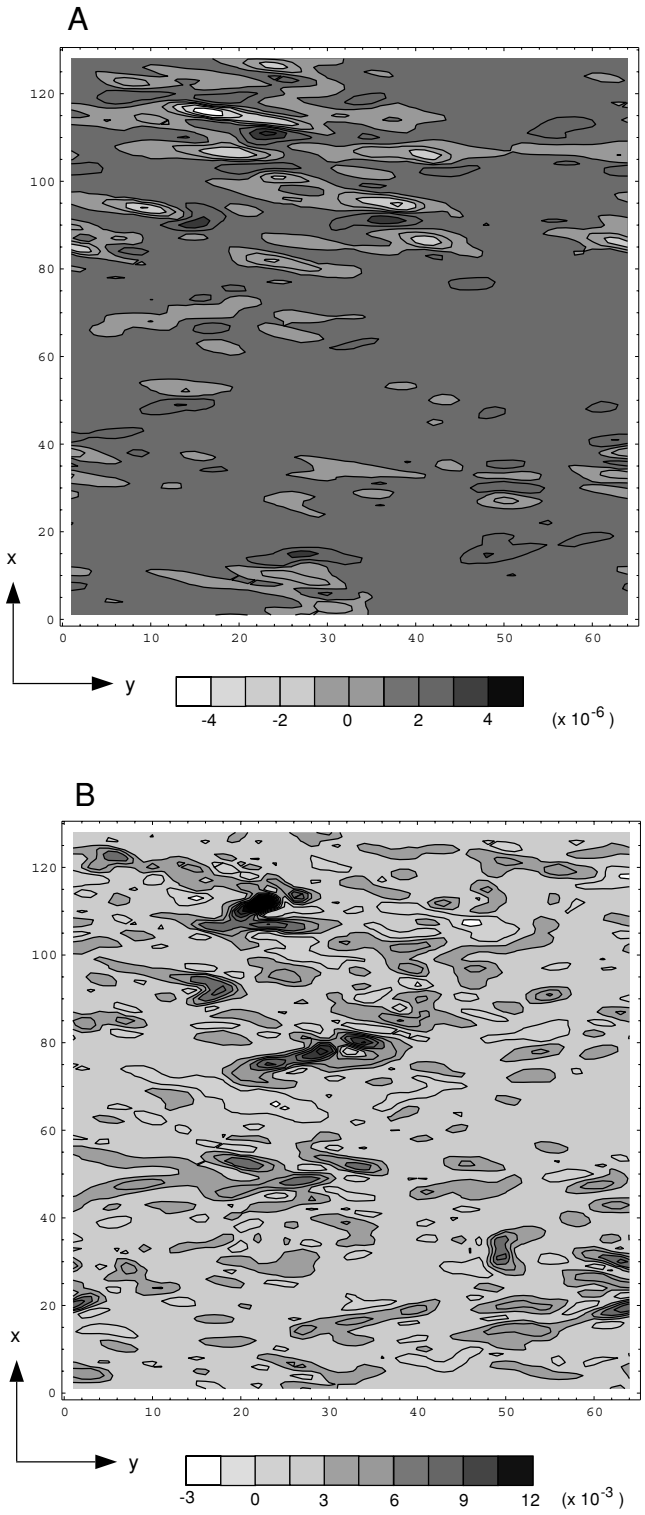

Figure 5. Estimates of the SGS quantities calculated from the DNS using (6) and (8). The shear stress T_{12} in (a) and the vertical heat flux I_3 in (b) are plotted on a horizontal surface through the middle of the computation volume. Comparisons with the predictions of the SGS models are made at the same time step.

that are much more compatible with those of the SGS heat flux in Fig. 5(b), although the peaks in the predicted heat flux are mislocated. The spatial correlation between the hyperdiffusion model and the SGS heat flux is $\gamma = 0.23$, which is worse than the correlation

Table 2. Dimensionless parameters.

Parameter	Symbol	Value
Magnetic Rossby	Ro	0.014
Rayleigh	Ra	0.0022 (a)
		0.0018 (b)
Elsasser	Λ	1.1
Magnetic Prandtl	P_{m}	6×10^{-5}
Roberts	q	6×10^{-5}

The Rayleigh number for (a) $\theta = 0$ and (b) $\theta = \pi/4$.

Table 3. Amplitude of SGS heat flux and stress.

Quantity	rms amplitude
T_{12}	1.62×10^{-6}
T_{13}	0.65×10^{-6}
T_{23}	4.67×10^{-6}
I_1	3.40×10^{-3}
I_2	19.2×10^{-3}
I_3	16.9×10^{-3}

obtained with the eddy-diffusion model. The poorer performance is due to the increased amplitude of the short-wavelength part of I_3, which is poorly correlated with the SGS estimate of I_3. While the hyperdiffusion model appears to reproduce the correct amplitude of Fourier components in I_3, it fails to predict the phase of these components correctly.

5.3 Predictions the Smagorinsky model

The constant C_S in the Smagorinsky model is adjusted to reproduce the rms amplitude of the SGS estimate of T_{12}. The value recovered by this procedure is $C_S = 0.12$, which is only slightly larger than

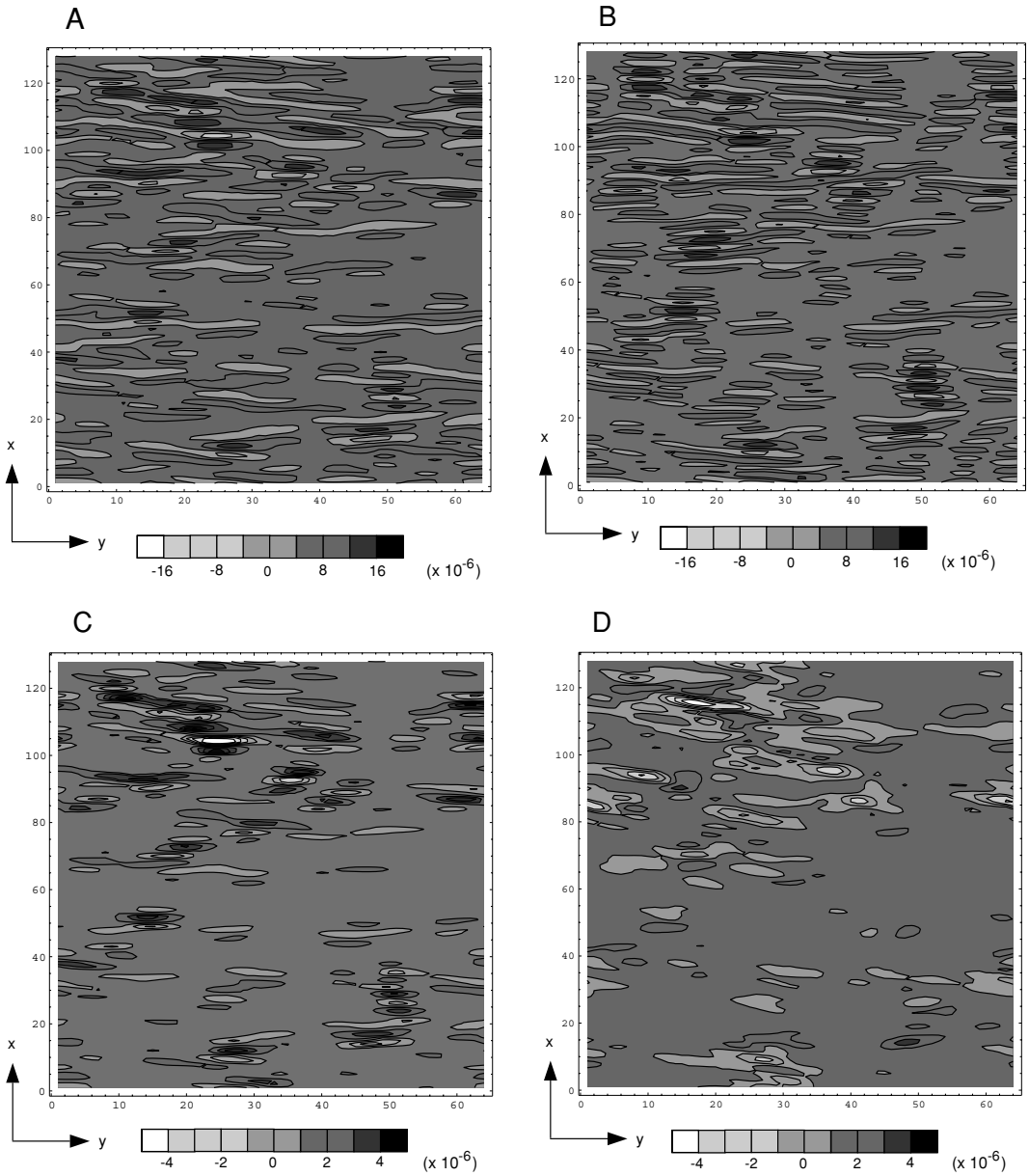

Figure 6. Predictions of the SGS models for shear stress T_{12}. The models include (a) the eddy-viscosity model, (b) the hyperviscosity model, (c) the Smagorinsky model and (d) the similarity model (see the text for the parameter values used in the model calculations).

Table 4. Summary of the eddy-diffusion models.

Model	Quantity	Amplitude ratio†	Correlation
Eddy viscosity	T_{12}	3.88	−0.24
	T_{13}	4.71	−0.07
	T_{23}	0.21	0.21
	I_1	6.72	−0.05
	I_2	0.38	0.39
	I_3	0.64	0.40
Hyperviscosity	T_{12}	3.88	−0.19
	T_{13}	4.82	−0.09
	T_{23}	0.15	0.17
	I_1	29.1	−0.09
	I_2	1.21	0.29
	I_3	0.94	0.23
Smagorinsky	T_{12}	1.00	−0.28
	T_{13}	1.53	−0.14
	T_{23}	0.03	0.28
	I_1	9.91	−0.14
	I_2	0.54	0.57
	I_3	0.82	0.41

† Model prediction divided by the SGS estimate from eq. (6) or eq. (8).

the value $C_S = 0.1$ customarily adopted in other applications (e.g. Moin & Kim 1982). The resulting prediction for T_{12} is shown in Fig. 6(c). Comparison with the SGS estimate in Fig. 5(a) reveals some consistent features, including the spatial variability of T_{12} and the long-wavelength structure, which places the largest stresses (positive or negative) in the same general location. However, the sign of the largest-amplitude stresses in the SGS estimate are negative, whereas the largest stresses in the Smagorinsky model are positive. Consequently, the spatial spatial correlation is poor ($\gamma = -0.28$).

Better predictions are obtained for the vertical heat flux I_3 (Fig. 7c). The turbulent Prandtl number $Pr = 0.14$ is chosen by matching the net heat flux in the prediction to the value calculated from the SGS estimate (Fig. 5b). The pattern of upwelling in the Smagorinsky model is similar to the prediction of the eddy-diffusivity model, although there is much more small-scale structure in the Smagorinsky model. The spatial correlation between the Smagorinsky model and the SGS estimate is $\gamma = 0.41$, which is only slightly better than the correlation obtained with the eddy-diffusivity model.

5.4 Predictions of the similarity model

Two filters must be specified to define the similarity model. The first is required to define the fields $\bar{\mathbf{V}}$, $\bar{\mathbf{B}}$ and $\bar{T}$, and the second is used to evaluate eqs (21) and (22) for the SGS heat flux and stress. We use a Gaussian filter with $\Delta = \pi/32$ to determine $\bar{\mathbf{V}}$, $\bar{\mathbf{B}}$ and $\bar{T}$, and adopt a Gaussian filter with a width of $4\Delta/3$ as the second filter. The width of the second filter is chosen on the basis of the numerical resolution required to de-alias the non-linear terms using the 3/2 rule (e.g. Canuto *et al.* 1988). For an effective grid spacing of Δ, the non-linear terms must be evaluated on a grid with spacing $2\Delta/3$. Thus a filter width of $4\Delta/3$ is twice as coarse as the grid used to evaluate the non-linear terms.

The Gaussian filters are applied by Fourier transforming the convolution integral in eq. (1). The Fourier components of the filtered field (say $\bar{\mathbf{V}}_k$) are related to the Fourier components of the unfiltered field by

$$\bar{\mathbf{V}}_k = \mathcal{G}(\mathbf{k}, \Delta)\mathbf{V}_k, \tag{41}$$

where

$$\mathcal{G}(\mathbf{k}, \Delta) = \mathrm{e}^{-\Delta^2 k^2/24} \tag{42}$$

is the Fourier transform of the 3-D Gaussian filter with width Δ. The same procedure is used for the second Gaussian filter, which gives

$$\widetilde{\bar{\mathbf{V}}}_k = \mathcal{G}(\mathbf{k}, 4\Delta/3)\bar{\mathbf{V}}_k. \tag{43}$$

Fourier components of the non-linear terms in the similarity model are evaluated using the pseudospectral method described in Section 4.

The definition of the similarity model in eqs (21) and (22) includes two constants C_T and C_I, which are used to adjust the amplitude of the predicted heat flux and stress. We use $C_T = 0.95$ and $C_I = 0.91$ to make the rms amplitudes of T_{12} and I_3 equal to the amplitudes of the SGS estimates. The resulting predictions for T_{12} and I_3 are shown in Figs 6(d) and 7(d), respectively. In both cases the predictions are remarkably similar to the SGS estimates in Fig. 5. The spatial correlation between the predictions and the SGS estimates exceeds 90 per cent for both T_{12} and I_3 (Table 5), and there is virtually no difference in these spatial correlations if the SGS estimates are separated into long- and short-wavelength parts. Comparable agreement is achieved in the other components of heat flux and stress, even though the amplitudes vary substantially with direction (see Table 3). Differences in the amplitudes of T_{ij} and I_i reflect the presence of anisotropy in the SGS estimates, so it is encouraging that the similarity model reproduces these amplitude differences. We return to this point in the next section.

Spatial correlations with the SGS estimates continue to be good when $\bar{\mathbf{V}}$, $\bar{\mathbf{B}}$ and $\bar{T}$ are defined using a more severe truncation at $\Delta = \pi/16$ (Table 5). This is somewhat surprising because the wavenumber $k_1 \approx 16$ separates the convectively stable and unstable regimes. If the structure of flow at $k_1 < 16$ is not to be representative of flow at $k_1 > 16$, then the extrapolation implicit in the similarity model may not be valid. Despite these concerns the results are quite good, although the rms amplitudes are smaller than the corresponding SGS estimates from eqs (6) and (8). This shortcoming can be corrected by adjusting the constants C_T and C_I. Of course, this assumes that the SGS estimates of the heat flux and stress are known. When the SGS estimates are not known, the constants C_T and C_I must be estimated from the resolved flow.

The choice of filters in the similarity method appears to affect the amplitude of the SGS predictions, but not the spatial correlation with the SGS estimates. For example, when $\bar{\mathbf{V}}$, $\bar{\mathbf{B}}$ and $\bar{T}$ are defined by spectral truncation rather than Gaussian filtering, the predictions of the similarity model increase in amplitude by about 30 per cent because these filtered fields have a larger amplitude. However, the spatial correlations of these two similarity predictions differ by less than 1 per cent when $\mathcal{G}(\mathbf{k}, 4\Delta/3)$ is used as the second filter in both calculations. This implies that the nature of the truncation used to define $\bar{\mathbf{V}}$, $\bar{\mathbf{B}}$ and $\bar{T}$ has only a small influence on the spatial distribution of the predicted SGS heat flux and stress. Different choices for the width of the filter in eq. (42) also affect the amplitudes, but again the spatial correlations are nearly unchanged. As an example, we consider another similarity prediction where $\bar{\mathbf{V}}$, $\bar{\mathbf{B}}$ and $\bar{T}$ are defined by spectral truncation at $k_i = 32$, and a narrower filter with Δ instead of $4\Delta/3$ is used in eq. (43). The amplitudes of the predicted SGS heat flux and stress decrease relative to the previous example, but the spatial correlations are not altered. These examples suggest that the predictions of the similarity model are robust with respect to the choice of filter. However, changes in the amplitude of the SGS predictions indicate that the constants C_T and C_I must be adjusted

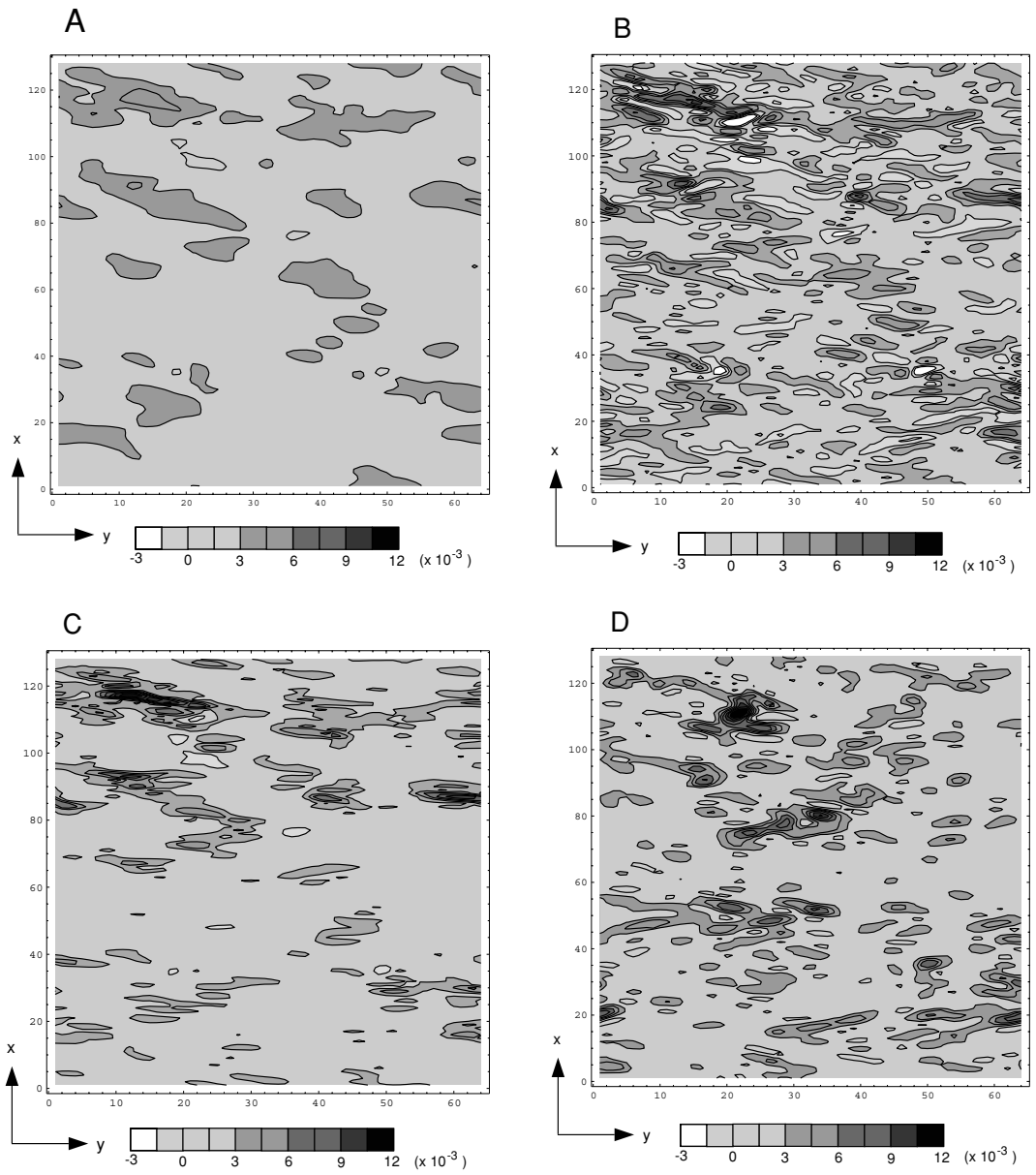

Figure 7. Predictions of the SGS models for vertical heat flux I_3. The models include (a) the eddy diffusion model, (b) the hyperdiffusivity model, (c) the Smagorinsky model and (d) the similarity model (see the text for the parameter values used in the model calculations).

for the problem of interest, preferably using information from the resolved fields.

6 DISCUSSION

The structure of convection in the DNS causes anisotropy in the SGS heat flux and stress (see Table 3). Evidence for a direction dependence is readily seen in the SGS heat flux, where I_1 is substantially smaller than I_2 and I_3. These particular differences are attributed to the plate-like temperature anomalies in Fig. 3, which produce relatively weak flow in the x-direction. None of the SGS models that rely on scalar eddy diffusivities can account for this anisotropy, so there is no single choice of model parameters that yields satisfactory results. The parameters of the model can be adjusted to match one component of the SGS estimates, but the remaining components are bound to be inaccurate. These difficulties are evident in Table 4, where the rms amplitudes of the model predictions are normalized by the amplitudes of the corresponding SGS estimates. For example, the eddy diffusion model overestimates I_1, but underestimates I_2 and I_3 when $\kappa_t = 7 \times 10^{-5}$. Choosing other values for the eddy diffusivity simply shifts all of the components of $\mathbf{I}$ to higher or lower values without altering their relative magnitude. Similar problems occur in the predictions of the hyperviscosity and Smagorinsky models.

The similarity model is much more successful in reproducing the anisotropy in the SGS estimates (Table 5). The amplitudes of the model predictions are in good agreement with the SGS estimates, particularly when $\bar{\mathbf{V}}$, $\bar{\mathbf{B}}$ and $\bar{T}$ are truncated at $\Delta = \pi/32$. The predictions of the similarity model underestimate the SGS quantities, but substantial improvements are possible if the model constants C_T and C_I are suitably adjusted. The fact that the relative amplitudes of the SGS estimates are reliably reproduced by the similarity model

Truncation	Quantity	Amplitude ratio†	Correlation
$\Delta = \pi/32$	T_{12}	1.00	0.92
	T_{13}	1.05	0.94
	T_{23}	0.86	0.87
	I_1	0.91	0.83
	I_2	0.97	0.84
	I_3	1.00	0.92
$\Delta = \pi/16$	T_{12}	0.69	0.88
	T_{13}	0.70	0.84
	T_{23}	0.47	0.75
	I_1	0.73	0.76
	I_2	0.51	0.80
	I_3	0.68	0.89

†Model prediction divided by the SGS estimate from eq. (6) or eq. (8).

means that the anisotropy in the SGS heat flux and stress is accurately modelled. More elaborate schemes to fine tune C_T and C_I should ensure a good match to the amplitude and spatial distribution of the SGS estimates.

Expressions for the SGS Lorentz force and magnetic induction are not evaluated in this study because both quantities are very small at the small spatial scales considered here. In principle, the similarity model is easily extended to account for these terms, but the success of the method depends on the validity of the underlying assumptions. In particular, it is assumed that unresolved flow at scales immediately below Δ has the greatest influence on the resolved scales. This is plausible for the SGS Lorentz force, but it may not be true for the SGS induction term. Analysis of the numerical geodynamo model of Kuang & Bloxham (1999) indicates that the largest contributions to the dipole field arise from small-scale flow with a local magnetic Reynolds number (R_m) of approximately $R_m \approx 1$ (Buffett & Bloxham 2002). If the truncation used in a numerical geodynamo model is too coarse to include the length-scales corresponding to $R_m \approx 1$, then the generation of the dipole field by motion at the resolved scales may not be representative of the induction by unresolved motion at $R_m \approx 1$. In this case the largest contribution to the dipole might come from flow at scales well below Δ. In order to accurately simulate the geodynamo without resorting to specialized models for the effects of magnetic induction at $R_m \approx 1$, it is necessary to resolve the flow down to scales where $R_m \approx 1$. Resolving smaller scales associated with viscous and thermal dissipation should be unnecessary if SGS models such as the similarity model can be successfully applied to the geodynamo.

Previous use of the similarity model in numerical simulations of homogeneous turbulence indicates that this model does not dissipate enough energy at the resolved scales (Meneveau & Katz 2000). In addition, backscattering of energy from the unresolved scales can cause instabilities in the numerical simulations. As a result, many studies combine the similarity model with a Smagorinsky model to enhance the dissipation of energy at the resolved scales and to ensure numerical stability (Vreman *et al.* 1997; Winckelmans *et al.* 2001). The geodynamo problem is somewhat different from conventional turbulence because most of the kinetic and magnetic energy generated by buoyancy at a particular scale is dissipated at that scale (Olson *et al.* 1999; Buffett & Bloxham 2002). This may make geodynamo simulations less vulnerable to numerical instabilities of the sort that arise in LES studies of homogeneous turbulence. On the other hand, non-linear interactions between the velocity and magnetic fields in geodynamo simulations may create new difficulties. Implementing the similarity model in geodynamo simulations should be relatively straightforward, but testing the validity of the model is a more difficult challenge.

The discussion so far has focused on the SGS heat flux and stress in the interior of the fluid. The influence of boundaries introduce complications that must be taken into account before these methods can be fully exploited in the geodynamo problem. Further complications arise when the method is applied in spherical geometries, although these difficulties are mainly technical in nature. For example, the integrals required to transform the convolution integral in eq. (1) to the spectral domain are more difficult to evaluate in spherical geometries, but the general approach does not change. Finally, we require methods for evaluating the constants in the similarity model. In this study the constants C_T and C_I are of the order of unity, so we might expect a reasonable first approximation using models with $C_T = C_I = 1$. More elaborate (and computationally expensive) schemes to adjust the model parameters may be necessary if the use of preset constants is insufficient.

7 CONCLUSIONS

Four subgrid-scale models are applied to the problem of magnetoconvection in the Earth's core and the results compared with estimates from a fully resolved DNS. Three of the models are based on eddy diffusivities and the fourth is the similarity model of Bardina *et al.* (1980). The models based on eddy diffusivities are incapable of reproducing the anisotropy in the SGS estimates of heat flux and stress. In addition, the predictions are often poorly correlated with the spatial distribution of the known SGS quantities. In contrast, the similarity model reproduces the anisotropy and gives a remarkably good match to the spatial distribution of the SGS estimates. Different choices of filters in the similarity model appear to influence the amplitude of the SGS predictions, but have relatively little influence on their spatial distribution.

Extensions of this method to account for the SGS Lorentz force and magnetic induction are straightforward, although the predictions for magnetic induction may be unreliable if the underlying assumptions of the method are not satisfied. An accurate description of the SGS magnetic induction requires a discretization that resolves the flow at scales where the local magnetic Reynolds number is of the order of unity. This resolution may be feasible with current computational resources. Reliable geodynamo simulations could then be realized with good SGS models for the heat flux and stress. The analysis here suggests that the similarity model offers a viable approach for achieving this goal.

ACKNOWLEDGMENTS

I thank Paul Roberts for comments on an early draft of this paper. Uli Christensen and an anonymous reviewer made many helpful comments and suggestions. This work is supported by an NSERC Research Grant.

REFERENCES

Bardina, J., Ferziger, J.H. & Reynolds, W.C., 1980. Improved subgrid scale models for large-eddy simulations, *Am. Inst. Aeronaut. Astronaut.,* Paper 80-1357.

Braginsky, S.I. & Meytlis, V.P., 1990. Local turbulence in the Earth's core, *Geophys. astrophys. Fluid. Dyn.,* **55,** 71–87.

Braginsky, S.I. & Roberts, P.H., 1995. Equations governing convection in

Earth's core and the geodynamo, *Geophys. astrophys. Fluid. Dyn.,* **79,** 1–97.

Buffett, B.A. & Bloxham, J., 2002. Energetics of numerical geodynamo models, *Geophys. J. Int.,* **149,** 211–221.

Busse, F.H., 2000. Homogeneous dynamos in planetary cores and in the laboratory, *Ann. Rev. Fluid Mech.,* **32,** 383–408.

Cantin, N., Vincent, A.P. & Yuen, D.A., 2000. Large-eddy simulations of thermal convection at high Rayleigh number, *Geophys. J, Int.,* **140,** 163–174.

Canuto, V.M. & Cheng, Y., 1997. Determination of the Smagorinsky–Lilly constant c_s, *Phys. Fluids,* **9,** 1368–1378.

Canuto, C., Hussaini, M.Y., Quarteroni, A. & Zang, T.A., 1988. *Spectral Methods in Fluid Dynamics,* Springer-Verlag, Berlin.

Christensen, U., Olson, P. & Glatzmaier, G.A., 1998. A dynamo model interpretation of geomagnetic field structures, *Geophys. Res. Lett.,* **25,** 1565–1568.

Christensen, U., Olson, P. & Glatzmaier, G.A., 1999. Numerical modelling of the geodynamo: a systematic parameter study, *Geophys. J. Int.,* **138,** 393–409.

Clarke, R.A., Ferziger, J.H. & Reynolds, W.C., 1979. Evaluation of subgrid-scale models using an accurately simulated turbulent flow, *J. Fluid Mech.,* **91,** 1–16.

Dobson, D.P., 2000. Fe-57 and Co tracer diffusion in liquid Fe–FeS at 2 and 5 GPa, *Phys. Earth planet. Inter.,* **120,** 137–144.

Germano, M., 1986. A proposal for a redefinition of the turbulent stresses in the filtered Navier–Stokes equations, *Phys. Fluid,* **29,** 2323–2324.

Glatzmaier, G.A., 2002. Geodynamo simulations: how realistic are they?, *Ann. Rev. Earth Planet. Sci.,* **30,** 237–257.

Glatzmaier, G.A. & Roberts, P.H., 1995. A three-dimensional convective dynamo solution with rotating and finitely conducting inner core and mantle, *Phys. Earth planet. Inter.,* **91,** 63–75.

Glatzmaier, G.A. & Roberts, P.H., 1996. An anelastic evolutionary geodynamo simulation driven by compositional and thermal convection, *Physica D,* **97,** 81–94.

Grote, E., Busse, F.H. & Tilgner, A., 2000. Effects of hyperdiffusion on dynamo simulations, *Geophys. Res. Lett.,* **27,** 2001–2004.

Krause, F. & Radler, H.-K., 1979. On the theory of the geomagnetic dynamo based on mean field electrodynamics, *Phys. Earth planet. Inter.,* **20,** 158–171.

Kuang, W. & Bloxham, J., 1997. An Earth-like numerical dynamo model, *Nature,* **389,** 371–374.

Kuang, W. & Bloxham, J., 1999. Numerical modelling of magnetohydrodynamic convection in a rapidly rotating spherical shell: weak and strong field dynamo action, *J. Comp. Phys.,* **153,** 51–81.

Leonard, A., 1974. Energy cascade in large-eddy simulations of turbulent flow, *Adv. Geophys.,* **18,** 237–248.

Lesieur, M. & Métais, O., 1996. New trends in large-eddy simulations of turbulence, *Ann. Rev. Fluid. Mech.,* **28,** 45–82.

Lilly, D.K., 1967. The representation of small-scale turbulence in numerical simulation experiments, in *Proc. IBM Scientific Computing Symp. Environ. Sci.,* IBM Data Processing Division, White Plains, NY, pp. 195–211.

Liu, S., Meneveau, C. & Katz, J., 1994. On the properties of similarity subgrid-scale models as deduced from measurements in a turbulent jet, *J. Fluid. Mech.,* **275,** 83–119.

Matsushima, M., 2001. Expression of turbulent heat flux in the Earth's core in terms of a second moment closure model, *Phys. Earth planet. Inter.,* **128,** 137–148.

Matsushima, M., Nakajima, T. & Roberts, P.H., 1999. The anisotropy of local turbulence in the Earth's core, *Earth Planets Space,* **51,** 277–286.

Meneveau, C. & Katz, J., 2000. Scale-invariance and turbulence models for large-eddy simulation, *Ann. Rev. Fluid. Mech.,* **32,** 1–32.

Moffatt, H.K., 1970. Turbulent dynamo action at low magnetic Reynolds number, *J. Fluid. Mech.,* **41,** 435–452.

Moin, P. & Kim, J., 1982. Numerical investigations of turbulent channel flow, *J. Fluid. Mech.,* **118,** 341–377.

Olson, P., Christensen, U. & Glatzmaier, G.A., 1999. Numerical modeling of the geodynamo: Mechanisms of field generation and equilibration, *J. geophys. Res.,* **104,** 10 383–10 404.

Orszag, S.A., 1971. Numerical simulation of incompressible flows within simple boundaries: I. Galerkin (spectral) representations, *Stud. Appl. Math.,* **50,** 293–327.

Roberts, P.H. & Glatzmaier, G.A., 2000. Geodynamo theory and simulations, *Rev. Mod. Phys.,* **72,** 1081–1123.

Rogallo, R.S. & Moin, P., 1984. Numerical simulation of turbulent flows, *Ann. Rev. Fluid. Mech.,* **16,** 99–137.

Shimizu, H. & Loper, D.E., 1997. Time and length scales of buoyancy-driven flow structures in a rotating hydromagnetic fluid, *Phys. Earth planet. Inter.,* **104,** 307–329.

Smagorinsky, J., 1963. General circulation experiments with the primitive equations, I. The basic experiment, *Mon. Weather Rev.,* **91,** 99–164.

St Pierre, M.G., 1996. On the local nature of turbulence in Earth's outer core, *Geophys. astrophys. Fluid. Dyn.,* **83,** 293–306.

Vocadlo, L., Alfe, D., Price, G.D. & Gillan, M.J., 2000. First principle calculations of the diffusivity and viscosity of liquid Fe–FeS at experimentally accessible conditions, *Phys. Earth planet. Inter.,* **120,** 145–152.

Vreman, B., Geurts, B. & Kuerten, H., 1997. Large-eddy simulations of turbulent mixing layer, *J. Fluid. Mech.,* **339,** 357–390.

Winckelmans, G.S., Wray, A.S., Vasilyev, O.V. & Jeanmart, H., 2001. Explicit-filtering large-eddy simulation using the tensor-diffusivity model supplemented by a dynamic Smagorinsky term, *Phys. Fluid.,* **13,** 1385–1403.

Zhang, K., 1994. On coupling between the Poincaré equation and the heat equation, *J. Fluid. Mech.,* **268,** 211–229.

Zhang, K. & Jones, C., 1997. The effect of hyperviscosity on geodynamo models, *Geophys. Res. Lett.,* **24,** 2869–2872.